Electronic Supplementary Material (ESI) for Nanoscale.
This journal is © The Royal Society of Chemistry 2023

Supplementary Information for

Combined Three Dimensional Locomotion and Deformation of Functional Ferrofluidic Robots

Xinjian Fan, Yunfei Zhang, Zhengnan Wu, Hui Xie, Lining Sun, Tao Chen, Zhan Yang

Corresponding Author: ***Tao Chen, Zhan Yang***

E-mail: ***chent@suda.edu.cn, yangzhan@suda.edu.cn;***

The PDF file includes:

Fig. S1 to Fig. S12.

Supplementary text

Legends for Movies S1 to S6.

SI References.

Other supplementary material for this manuscript includes the following:

Movie S1. Simulation and experiment results of the 2D motion control of the ferrofluidic robot.

Movie S2. Simulation and experiment results of the 3D motion control of the ferrofluidic robot.

Movie S3. Experiment results show deformed ferrofluidic robots can be used as microfluidic inducers.

Movie S4. 3D locomotion of ferrofluidic robots for navigation and hitting missions.

Movie S5. Applications of ferrofluidic robots based on combined 3D locomotion and deformation.

Movie S6. Experimental application of pig lung bronchus biology.

Notice: The content displayed at the top of the video indicates the speed at which the video plays.

Supplementary Note 1. Supplementary Figures

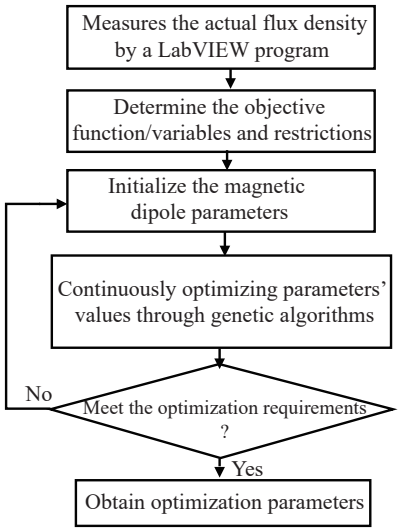

Supplementary Figure 1. Optimization process for precise electromagnetic coil modeling.The optimization flowchart for the entire dipole model is initially derived from the relevant dipole formula and the parameters that need to be determined. Subsequently, a LabVIEW program is used to measure the relationship between voltage and distance, and a genetic algorithm is employed to solve the optimization problem by minimizing the errors between the measured and evaluated data.

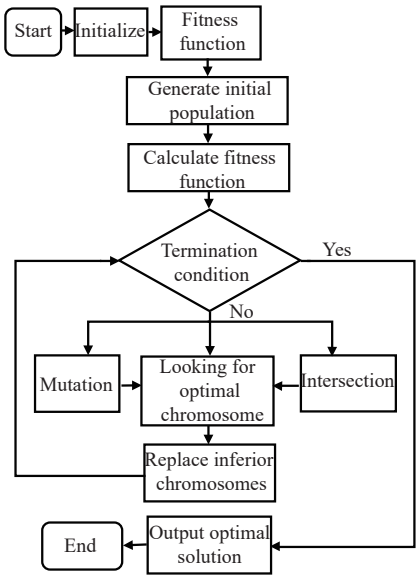

Supplementary Figure 2. The fundamental implementation process of a genetic algorithm[1]. The flowchart for deploying genetic algorithms involves several steps, including defining the problem, selecting appropriate genetic operators, initializing the population, evaluating the fitness of the population, selecting the best-fit individuals, and generating new populations through the process of crossover and mutation. The algorithm continues to iterate until a satisfactory solution is found.

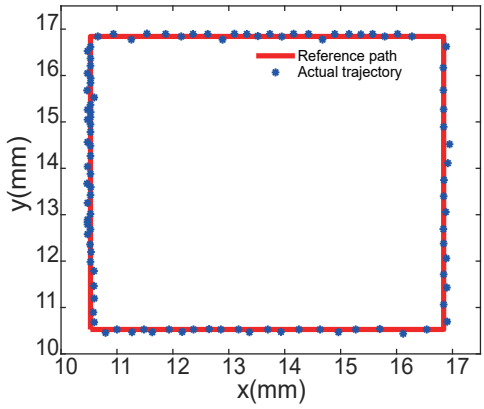

Supplementary Figure 3. The tracking results of a ferrofluidic robot on a two-dimensional square trajectory. The rectangular trajectory used in the experiment had dimensions of 6.5 mm $\times$6.5 mm, with the red line representing the preset trajectory and the blue dots and lines representing the actual trajectory of the robot during the experiment.

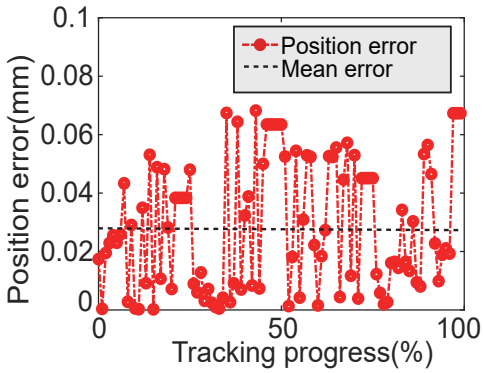

Supplementary Figure 4. Tracking error on a two-dimensional square trajectory. The error in the two-dimensional rectangular trajectory was found to fluctuate between 0 and 0.07mm, with an average error of approximately 0.028mm. These findings demonstrate the precision and accuracy of the robot in following the designated path, and can be used to inform future research and development in the field of autonomous vehicle navigation.

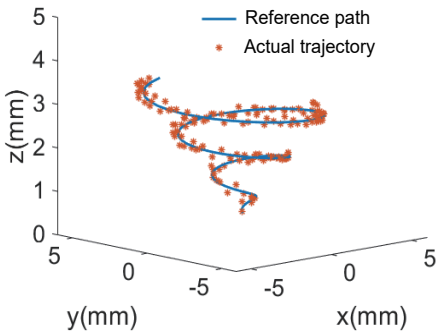

Supplementary Figure 5. The tracking results of a ferrofluidic robot on a 3D involute trajectory.The involute trajectory used in the experiment had dimensions of 8 mm$\times$8 mm$\times$4 mm, with the blue solid line representing the pre-designed trajectory and the red dotted line representing the actual trajectory of the robot during the experiment.

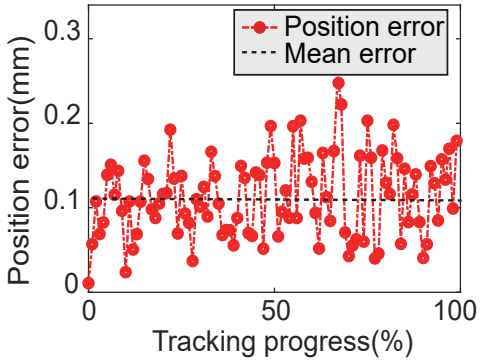

Supplementary Figure 6. Tracking error on a three-dimensional involute trajectory. The tracking error on a three-dimensional involute trajectory exhibits a range of 0.01 mm to 0.24 mm, with an average error of 0.11 mm.

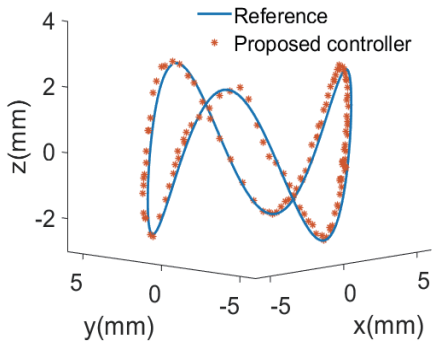

Supplementary Figure 7. The tracking results of a ferrofluidic robot on a three-dimensional saddle shape trajectory. The saddle-shaped trajectory has dimensions of 8 mm $\times$ 8 mm $\times$ 6 mm (length $\times$ width $\times$ height). The blue solid line represents the pre-designed trajectory, while the red dotted line depicts the actual trajectory of the robot during the experiment.

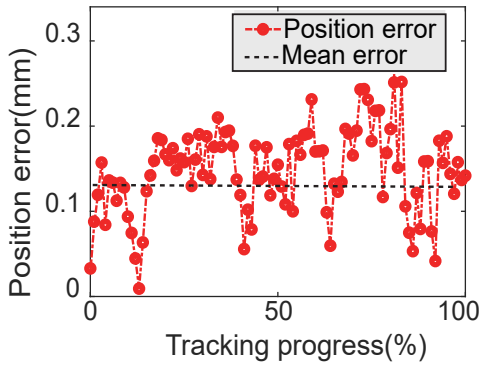

Supplementary Figure 8. Tracking error on a three-dimensional saddle shape trajectory.The tracking error on a three-dimensional saddle-shaped trajectory varies between 0.01 mm and 0.25 mm, with an average error of 0.13 mm.

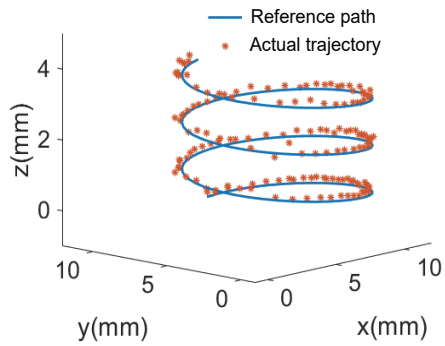

Supplementary Figure 9. The tracking results of a ferrofluidic robot on a 3D spiral trajectory. The size of the spiral trajectory is 10 mm$\times$10 mm$\times$4 mm, the blue solid line is the pre-designed trajectory, and the red dotted line is the actual trajectory of the robot during the experiment.

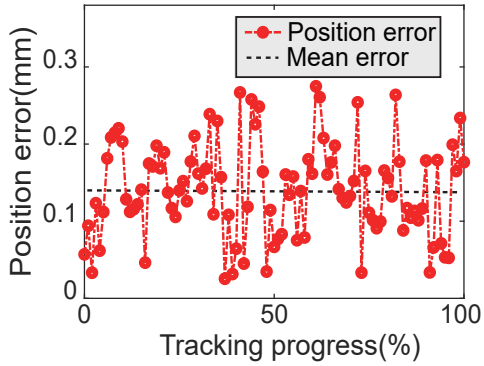

Supplementary Figure 10. Tracking error on a 3D spiral trajectory. The tracking error on a 3D spiral trajectory ranges from 0.02 mm to 0.28mm, with an average error of 0.14mm.

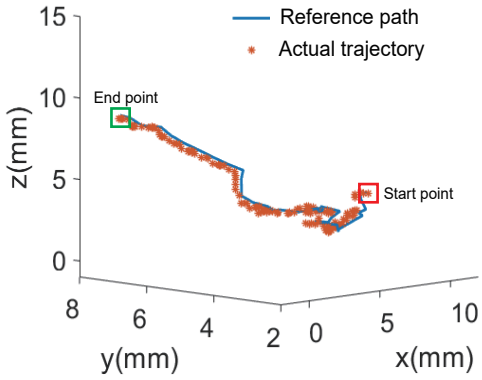

Supplementary Figure 11. Planned path and actual motion trajectory of a ferrofluidic robot in a 3D maze. The blue solid line is the pre-designed trajectory, and the red dotted line is the actual trajectory of the robot during the experiment.

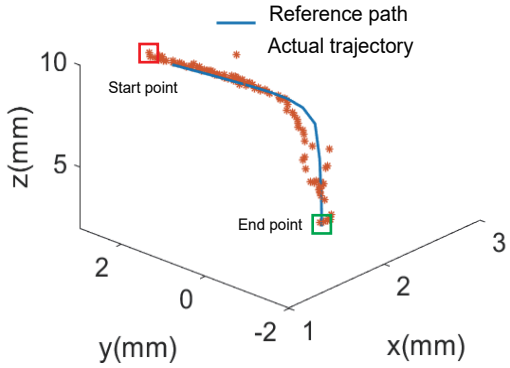

Supplementary Figure 12. The planning path and motion trajectory of robots in dynamic target hitting tasks. The blue solid line is the pre-designed trajectory, and the red dotted line is the actual trajectory of the robot during the experiment.

Supplementary Note 2. Supplementary Texts.

Design of sliding mode controller

Let x denote the current position of the robot and x_d be the desired position or target point. The error e is defined as $e = x_d - x$. The general formulation of sliding mode control is represented as $x = \dot{f(x)} + u$, where $\dot{e} = \dot{x}_d - \dot{x} = \dot{x}_d - f(x) - u$. The objective is to guarantee that x converges to x_d and the absolute value of $f(x)$ remains less than $p(x)$, where $p(x)$ is a predefined bound function.

The structure of the sliding mode controller employed in this study is defined by the following equation[2]:

$$u = \dot{x}_d + ke + \rho \frac{|e|}{e} \tag{1}$$

where u is the control action, $\dot{x}_d$ is the desired speed, k is the proportional gain, e is the error, and ρ is a positive constant.

The stability of the controller is subsequently validated. Letting $V_{(e)} = \frac{1}{2}e^2$ and then $\dot{V}(e) = e\dot{e}$, and substituting this into Equation 1, we arrive at Equation 2:

$$\dot{V}_{(e)} = -ke^2 - ef(x) - \rho|e| \tag{2}$$

Considering that $|f(x)| < p(x)$ and substituting this into the previous equation, we obtain $\dot{V}(e) \leq -ke^2 = -2kV(e)$. Assuming that the function $S_{(t)} > 0$ remains consistently positive, we can formulate a first-order linear non-homogeneous equation, as shown in Equation 3:

$$\dot{V}_{(e)} + 2kV_e = -S_{(t)} \tag{3}$$

The general solution to the above equation is $V_{(t)} = V_{(0)}\, exp(-2kt) - exp(-2kt) \int_0^t exp(2k\tau) S_{(\tau)} d\tau$. Since the latter part of the general solution must be positive, we can conclude that $V_{(t)} \leq V_{(0)}\, exp(-2kt)$. On substituting all the instances of V with error e, we arrive at Equation 4:

$$|e_{(t)}| \leq |e_{(0)}| exp(-2kt) \tag{4}$$

From Equation 4, it is evident that the sliding mode controller utilized in this study exhibits exponential stability and exceptional robustness. In Equation 1, the expression $\frac{|e|}{e}$ can be defined as follows:

$$\frac{|e|}{e} = \begin{cases} 1, & e > 0 \\ 0, & e = 0 \\ -1, & e < 0 \end{cases}$$

The abrupt change in the value of error e around 0 potentially impacts the smooth control of the system. Consequently, the expression is modified to $\frac{|e|}{e} = \frac{2}{1+exp(-m_s e)} - 1$, where m_s is an adjustable coefficient, employed to modulate the speed at which the function transitions from -1 to 1 in proximity to 0.

Besides, to address the singular value point problem during the control process of the magnetic actuation system, we utilize a decoupling control method for the xy and z axes. This method involves independent control of the top view trajectory and the main view trajectory, enabling effective 3D motion control of the ferrofluidic robot (Fig. 2D).

Supplementary Note 3. Supplementary Movies.

Movie S1. Simulation and experiment results of the 2D motion control of the ferrofluidic robot. This video shows the simulation and experimental motion results of ferrofluidic robots when tracks two-dimensional trajectories. The trajectory shape is circular in simulation, while the corresponding experimental trajectory varies between rectangular and circular shapes.

Movie S2. Simulation and experiment results of the 3D motion control of the ferrofluidic robot. The video showcases the simulation and experimental results of robots performing 3D trajectory tracking tasks. The simulated trajectory takes the form of a three-dimensional polyline, while the experimental trajectories include 3D polylines, involutes, spirals, and saddle trajectories.

Movie S3. Deformed ferrofluidic robots as microfluidic Inducer. This video showcases the deformed ferrofluidic robots can be used for pumping liquids in network-like structures such as blood vessel and for controlled mixing of various fluids. The video highlights their potential applications in fields such as microfluidics and lab-on-a-chip technology.

Movie S4. 3D locomotion of ferrofluidic robots for hitting missions. The video showcases the process of robots navigating complex 3D mazes, avoiding obstacles, and hitting both static and dynamic targets. The video emphasizes the robots' flexible mobility and high control accuracy during these tasks.

Movie S5. Applications of ferrofluidic robots based on combined 3D locomotion and deformation. In this video, we demonstrate the versatility of ferrofluidic robots for various tasks, thanks to their powerful deformation and motion abilities. Firstly, the video showcases the potential of ferrofluidic robots in controlling microchemical reactions. Next, the robot is applied to three-dimensional manipulation of small objects. Finally, it is demonstrated that ferrofluidic robots can be used for selective blockage of blood vessels. These applications highlight the potential of ferrofluidic robots for use in diverse fields, such as micro- and nano-manufacturing, biomedicine, and micro-surgery, where precise control and manipulation are essential.

Movie S6. Experimental application of pig lung bronchus biology. The video shows the overall flow of the robot entering the pig's lung bronchus to remove impurities, effectively demonstrating the robot's ability to remove impurities within complex organic structures. Intelligent control of robot movement may provide new avenues for medical treatment, especially in the case of removing impurities from organs, precisely targeted. Experimental design can lead to advances in the field of medical robotics that have the potential to revolutionize specific surgical and therapeutic procedures.

Supplementary References

[1] Srinivas M., Patnaik L. M. Genetic algorithms: A survey. *computer*, 1994, 27(6), 17-26.

[2] Edwards C, Spurgeon S. Sliding mode control: theory and applications[M]. *Crc Press*, 1998.